Unveiling the Importance of Non-Dominant Facets in (111)-Dominated Perovskite Films

Bo Zhou [a, b], Pei Zhao [d], Junxue Guo [a, e], Shuaifeng Hu [f], Xin Guo [a, b], Jiewei Liu [a, *], Can Li [b, c, *]

a State Key Laboratory of Photoelectric Conversion and Utilization of Solar Energy, Dalian Institute of Chemical Physics, Chinese Academy of Sciences, Dalian 116023, China

b University of Chinese Academy of Sciences, Beijing 100049, China

c State Key Laboratory of Catalysis, Dalian Institute of Chemical Physics, Chinese Academy of Sciences, Dalian 116023, China

d Research Center for Computational Science, Institute for Molecular Science, Okazaki 444-8585, Japan

e School of Chemistry and Materials Science, University of Science and Technology of China, Hefei 230026, China

f Clarendon Laboratory, Department of Physics, University of Oxford, Parks Road, Oxford OX1 3PU, U.K.

* Corresponding author.

E-mail: jwliu@dicp.ac.cn ; canli@dicp.ac.cn

Keywords: perovskite, (111)-dominated, facet distribution, facet heterogeneity, solvent regulation, diffraction

ABSTRACT: While (111)-dominated perovskite films hold potential for high-stability solar cells, most studies have primarily focused on modulating the (111) facets, overlooking the distribution and formation mechanism of the non-dominant (100) facets. In this study, we delve into (111) orientation via solvent regulation and investigated the evolution of facet distribution using various diffraction techniques. The findings reveal that simply stacking (111) facets does not inherently enhance solar cells; Instead, the distribution of non-dominant (100) facets in (111)-dominated films significantly influence both photoelectric property and stability. These observations highlight the critical need to manage the interplay between dominant and non-dominant facets. The study further offers strategies for addressing facet heterogeneity to achieve uniform facet distribution. This research provides a

comprehensive framework for understanding (111)-dominated perovskites and offer valuable guidance for designing high-performance perovskite solar cells.

1. INTRODUCTION

Orientation management of perovskites has garnered significant attention in recent years and has been widely applied in photovoltaic devices.[1] In principle, the (111) facet offers better resistance to moisture, providing superior environmental stability.[2] Early research for two-step methods typically produced films with a strong (111) diffraction peak, which were still considered randomly oriented rather than (111)-dominated due to their existing (100) peak and poor device performance.[3,4] Recent studies using wide-angle X-ray scattering (GIWAXS) to confirm (111)-dominated perovskite films have revealed that the (100) facets persist and cannot been completely eliminated.[5,6] These studies generally believed that these (100) facets do not negatively impact solar cell performance and that the dominant (111) orientation ultimately enhances power conversion efficiency (PCE). The comparable (111)/(100) facet proportions observed in both early and recent studies suggest that the impact of non-dominant (100) facets requires deeper investigation. Additionally, the limited reports on tunability of (111) orientation has hindered the development of universal two-step methods for (111)-dominated perovskites, emphasizing the need for a comprehensive framework to understand facet growth.

Here, we achieved a series of (111)/(100) facet proportions by adjusting the solvent ratio in the PbI_2 precursor, revealing that facet distribution in the two-step method is related to solvents and intermediate phases. Ultimately, the (111) dominance depends on the intensity of PbI_2 in the first deposition step, owing to parent-child mechanism. From the (111)-dominated films we obtained, we discovered that stronger (111) peaks or a higher (111)/(100) facet proportions do not necessarily correspond to higher PCE. Instead, it is the overlooked distribution of coexisting non-dominant (100) facets that plays a critical role in device performance. Compared to previous studies that mainly focused on the out-of-plane stacking of (111) facets, we employed a series of diffraction techniques to accurately and comprehensively analyze the vertical distribution of (111) and (100) facets. It was found that in (111)-dominated films, (100) facets are not randomly distributed, but enriched at the top and bottom surfaces, forming a vertical gradient hetero-facet structure. This unique (111)-(100) textured distribution ultimately induces uneven band alignment and contributes to the instability of the device. Gaining insights into this aspect is a key for deciphering facet distribution mechanisms and comprehending the facet heterogeneity in perovskite films. Additionally, the charge pitfalls caused by facet heterogeneity are not sensitive to the facet proportions or facet quantity but rather are closely related to their vertical distribution. Finally, we suggested that

this issue can be tackled with a fine-tuned composition regulation, establishing a coherent relationship between the facet distribution and the device performance.

2. RESULTS AND DISCUSSION

Construction of (111)-Dominated Orientation

To achieve tunable facet orientation, we employed a solvent regulation strategy. By altering the dimethyl sulfoxide (DMSO) amount in the conventional PbI_2 precursor solution, we found that solvent amount regulation significantly affected the proportion of (111) peaks (Figure 1A). This explains the inconsistency in XRD patterns of control films across different studies, as DMSO amount varies in each case. By keeping the total solvent amount constant and partially replacing DMSO with N-Methyl pyrrolidone (NMP), we were able to achieve a range of (111)/(100) facet proportions, with a prominent (111) diffraction peak is clearly observed at a DMSO:NMP ratio of 1:1, as shown in Figure 1B. The ratios of DMF:DMSO:NMP varied from 910:90:0 to 910:45:45, with the corresponding changes in crystal sizes and

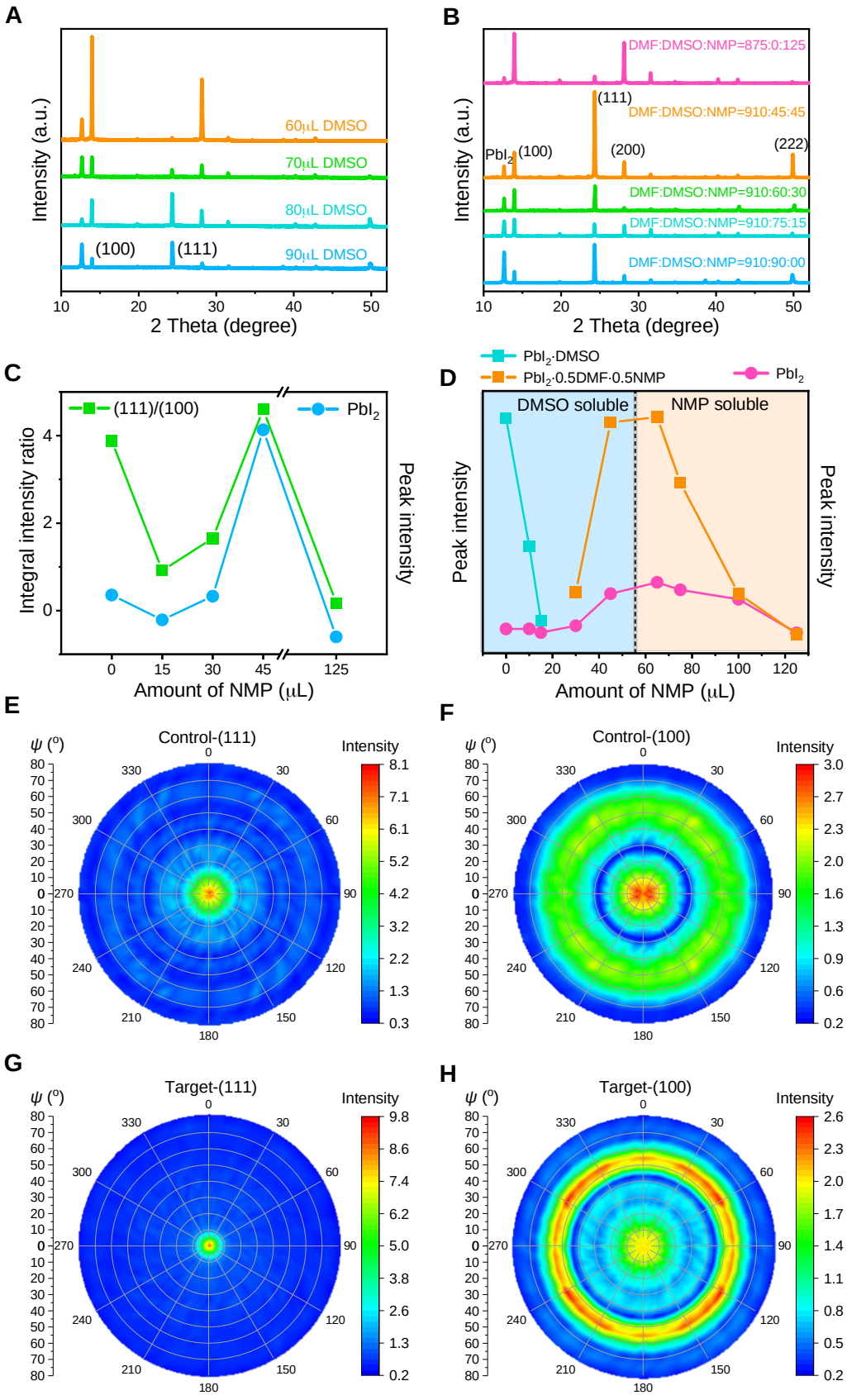

Figure 1. (A) XRD patterns for perovskite films with varied DMSO amounts. (B) XRD patterns for perovskite films with varied ternary solvent ratios. (C) Integral intensity

ratios of (111)/(100) and peak intensity of PbI_2 with varied NMP amounts. (D) Peak intensity variation for both intermediates and PbI_2 with different NMP content. Pole figure measurements along the (E, G) (111) facet and (F, H) (100) facet for the control and target films.

morphology detailed in Figures S2–S3 and Table S1.

Here, we used the solvents with DMF:DMSO:NMP = 910:90:00 as the control condition, and DMF:DMSO:NMP = 910:45:45 as the target condition. To discuss the impact of solvent on facet orientation, XRD was performed on PbI_2 and perovskite films with varying NMP proportion (Figure 1B, and Figure S4). The control film showed strong peaks of residual PbI_2 and the $(111)_{FAPbI_3}$, consistent with previous reports,[7] which is commonly regarded as a random distributed films with high (111) facet proportion. The XRD pattern of the target film is dominated by the (111) facet, with an intensity about five times greater than that of the (100) facet. Figure 1C further suggests that the preferred perovskite orientation is closely tied to the main lattice of first-step PbI_2, in line with literature reports.[8] The crystallographic alignment between $(001)_{PbI_2}$ and $(111)_{FAPbI_3}$, as shown in Figure S5, minimizes lattice mismatch energy, promoting the parallel growth of the (111) facet on $(001)_{PbI_2}$. Moreover, the first-step PbI_2 peak depends on the solvent and intermediate phases, as depicted in Figure 1D. Further diffraction analysis of the solvent intermediates reveals that the XRD peak at ~8.1° corresponds to the PbI_2•0.5DMF•0.5NMP intermediate phase,[9] with intensity depending on solvent ratio in Figure S6. It can be seen that the crystallinity of PbI_2 depends on the crystallinity of PbI_2•0.5DMF•0.5NMP. The two-step method is a sequential deposition process, making it natural to associate films with specific (111) orientations with the adjustment of PbI_2 films during the first deposition step. Since solvent regulation directly affects the PbI_2 solution in this step, it is also closely linked to the formation of solvent-mediated intermediate phases. Additionally, operational conditions also influence the orientation, as shown in Figure S7.

The difference between the control and target films lies in the enhanced crystallinity of the (111) peak in the latter. The (111)/(100) facet proportion is slightly higher in the target films. To further confirm the (111)-dominance of the target film, pole figure measurements were conducted (Figure 1E–1H, and Figure S8). Figure S9 provides schematic examples illustrating the relationship between pole figures and crystal orientations. In an out-of-plane (111)-oriented film, the (100) diffraction ring appears at 54.7° (the interplanar angle ψ), and vice versa.[10] The control film exhibits a random orientation because both the (111) and (100) diffraction rings produce at the center. This is a clear demonstration that in the target films, the (100) diffraction ring at 0° weakens, while the (100) diffraction ring shifts towards 54.7°, indicating a transition from a random distribution to a preferential (111) orientation. Besides, more centered

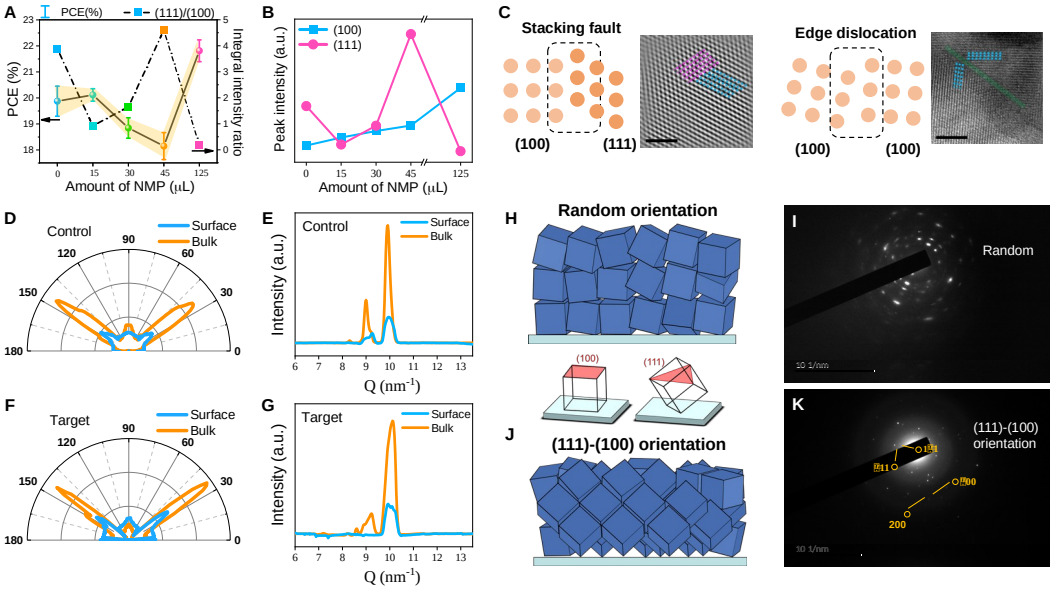

diffraction signals indicate stronger preferential orientations, which confirms that the target films are (111)-dominated, as evidenced by almost a central diffraction point signals in the target sample.[11]

Analysis of Non-Dominant (100) Facet Distribution

While NMP assistance resulted in a (111)-dominated structure, the PCE changed in the opposite way (Figure 2A and Figure S10), where the target perovskite solar cells (PSCs) show an average PCE of only 18.1%, compared to 19.7% for the control PSCs. This suggests that other critical factors are limiting the photovoltaic performance of PSCs. The variations of specific photovoltaic parameters are shown in Figure S11.

Figure 2. (A) The PCE distribution of PSCs with varied NMP amounts, compared to the (111)/(100) ratio variation. (B) The intensity of the (111) and (100) peaks with varied NMP amounts. (C) Schematics show two typical GBs defects that exist in the target film, and corresponding TEM images of the GBs defects (scale bar: 5 nm). (D, F) Radially integrated intensity plots along the $FAPbI_3$-(100) ring of the control and target perovskite films. (E, G) The 1D GIWAXS of the two films derived from the corresponding 2D GIWAXS patterns. The schematic illustrations between random (H, I) and (111)-(100) orientations (J, K) with ITO substrate, and the corresponding selected area electron diffraction (SAED) patterns (scale bar: 10 1/nm).

As observed in Figure 2A, The trend in PCE variation appears to be almost inversely correlated with the (111)/(100) ratio. This led us to investigate the overlooked (100) facets. Most (111)-dominated films inevitably contain some (100) facets, and it was previously believed that these (100) facets would

not significantly affect device performance, with the dominant (111) orientation expected to enhance PCE. However, in this work, it seems no longer to be the case. From Figure 2B and Figure S12, the peak intensities of (100) facets gradually increase, suggesting that NMP enhances the crystallographic structures of both (111) and (100) facets in the target film, with (111) being favored, ultimately resulting in a (111)-dominated orientation with mixed (100) facets. Transmission electron microscopy (TEM) clearly identifies two types of grain boundary (GB) defects in the target film caused by facet heterogeneity between (111) and (100) facets: stacking faults and edge dislocations.[12] These defects may act as charge recombination centers, trapping free charges, together contributing to reduced device performance.

Based on the analysis of the existing (100) facets, we need to reconsider the diffraction data. Both XRD and pole figures reflect the overall distribution, which is clearly insufficient for a detailed understanding. Here, we employed GIWAXS to study the distribution of crystal facets along the vertical direction by adjusting the incident angle, enabling surface and bulk-level investigations (Figure S13). The depth-dependent preferential orientations in the films are better visualized in Figure 2D and 2F. Both films show streaks at 36° and 144°, but the target film has stronger streaks in both the surface and bulk, indicating a (111)-dominated orientation. While the (111) orientation remains unchanged at the surface, the PbI_2 diffraction ring disappears, and the (100) plane at 90° exhibits an intensity reversal. This suggests that from bulk to surface, (100) facets strengthen as (111) facets weaken, leading to (100) facet enrichment at the surface. The 1D GIWAXS spectra exhibit the same trend (Figure 2E and 2G). While the PbI_2 peak in the bulk of the target film is substantially higher, it almost disappears at the surface, creating conditions for the (100) facet to become enriched at the surface by suppressing the epitaxial growth of the (111) facet through PbI_2. Although the control film exhibits a random orientation, it has a more uniform distribution between the surface and bulk in the vertical direction compared to the target film. This proves that the key factor in improving PCE is not the dominant orientation but the uniform distribution of facets within the film.

The differences in orientation between the two films can be better understood through the schematic illustrations in Figure 2H-2K. Randomly oriented stacking is less compact, often leading to vacancies and voids, as detailed in Figure S14. The target film represents a hybrid orientation, predominantly (111) with non-dominant (100) facets. Bright-field TEM images reveal tightly packed stacking, but the SAED patterns show two sets of diffraction spots. The domains of (100) facet stacking mismatch with those of (111) facet stacking, leading to significant GB defects, which have an immeasurable impact on the photovoltaic properties.

Mechanism of Facet Distribution and Its Relationship with Intermediate Phase

To comprehensively shed light on the distribution of (100) and (111) facets in the target film, we used GIXRD to explore the distribution of the facets both at the upper and lower interfaces. This revealed that (111) facets are dominant in bulk, while (100) facets are enriched at the surface and bottom (Figure 3A-3F and Figures S15-S16). Figure S17 and Table S2 shows the X-ray penetration depths at various incidence angles. The bottom interface formation is shown in Figure S16. At an incident angle of 0.5°, the (111)/(100) ratio is less than 1. As the incident angle increases, the (111) peak grows significantly, and the ratio gradually exceeds 1. In stark contrast, the control film exhibits a consistently dominant (111) peak from the surface to the bottom. Combining the data from inverse pole figures (IPF), we can observe the evolution of facet orientation. Similar to pole figures, the pole density values and the concentrated pole locations in IPFs are used to evaluate the degree of oriented growth in the film. Higher density values and denser pole locations indicate better crystal orientation. Figure 3B and 3C further confirm that films formed in a binary solvent system exhibit random orientations. When NMP is introduced into the DMF/DMSO solvent system, it initially reshuffles the facet distribution, leading to a non-dominant configuration. As the NMP content increases, the (111) orientation gradually strengthens, while the (100) facets become increasingly enriched at the top and bottom interfaces. The variation trend is illustrated in Figure S18. In addition to being (111)-dominant, the target is better described as having a (111)-(100) textured distribution (Figure S19).

Next, we examine the underlying origin in more detail. GIWAXS pattern of the unannealed target film (Figure S20) shows a uniform distribution between surface and bulk, indicating that facet distribution changes occur during the annealing process. In Figure S6 and S21, when the NMP ratio is low, the intermediate phase is predominantly PbI_2·DMSO. As the NMP ratio increases, PbI_2·DMSO completely disappears, transitioning to PbI_2·0.5DMF·0.5NMP phase. A competition exists between the two intermediate phases, influencing the final crystallographic orientation. This corresponds precisely to the early-stage shuffling process for facet

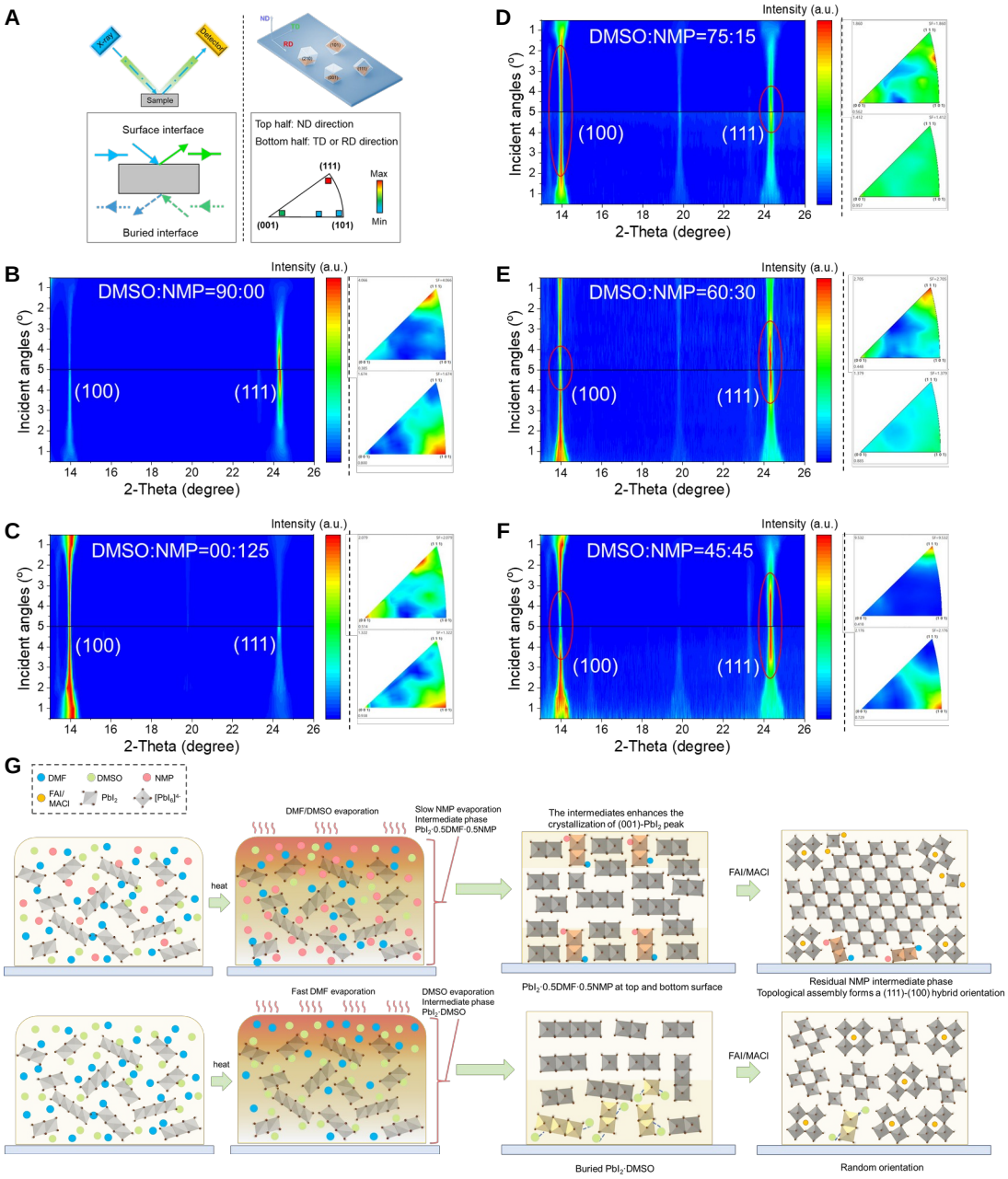

Figure 3. (A) The schematic diagrams of GIXRD and IPF characterization. (B-F) The 2D-GIXRD and IPF spectra of films with different solvent ratio. (G) The schematic illustration of the two-step crystallization processes with or without NMP assistance.

distribution shown in the IPFs, which highlights the critical role of the intermediate phase in solvent regulation (Table S3). As previously described, during PbI_2 deposition, the crystallinity of PbI_2 is influenced by the crystallinity of the PbI_2•0.5DMF•0.5NMP intermediate phase, while the growth of the (111) facet is also dependent on the crystallinity of PbI_2, forming a continuous

regulation process. The TEM data in Figure S22 demonstrate that with NMP intervention, PbI_2 exhibits improved ordering and enhanced crystallinity, transitioning from a heterogeneous to a homogeneous state. The well-crystallized PbI_2•0.5DMF•0.5NMP framework acts as a crystallization template, facilitating the transition to PbI_2, promoting its crystallization while suppressing the growth of the original (100) facets. This establishes the fundamental conditions for (111) facet dominance.

However, NMP's role in orientation growth is a double-edged sword. Compared to DMSO, NMP exhibits a strong affinity for FAI, as shown in Figure S23 and Table S4. This interaction enhances the penetration of organic salts, accelerating intramolecular exchange. Additionally, the expanded interlayer spacing provides more nucleation sites, favoring the formation of the thermodynamically preferred low-surface-energy (100) facet.[13,14] This explains the presence of the non-dominant (100) facet in the films.

Since the PbI_2•0.5DMF•0.5NMP intermediate phase simultaneously promotes the conversion of PbI_2, facilitating (111) facet dominance, while also energetically favoring (100) facet growth, its role under the target conditions appears to be more complex. As the result, the PbI_2•0.5DMF•0.5NMP intermediate phase is similarly concentrated at the top and bottom interfaces (Figure S24), owing to the high boiling point of NMP (203°C). During annealing, NMP tends to remain buried and incompletely evaporates, leaving residues at the upper and lower interfaces. In the second step, when organic cations are introduced into the PbI_2 lattice, NMP facilitates the FAI·NMP·PbI_2 complex for the low-surface-energy (100) facets.[9] The enrichment of (100) facets at both the top and bottom follows the same trend to the NMP intermediates, leading to the unique (111)-(100) textured distribution. The differences in the crystallization process are illustrated in Figure 3G. Experimental evidence regarding the crystallization process evolution can be found in Figures S24–S28. Figure S29 further explores alternative solvents, none of which exhibit the same evolution as NMP, confirming that the unique texture distribution arises from the distinct intermediate phase properties of NMP. Finally, density functional theory (DFT) calculations demonstrate that the (111) orientation in the two-step process is primarily governed by kinetic factors rather than thermodynamic control (Figure S30).

Relationship Between Facet Distribution and Photoelectric Property

We now understand that the target film does not have a uniform distribution, but instead displays a specific textured distribution of facets. The impact of facet enrichment at the surface and bottom on device performance remains unclear, necessitating the need to correlate the crystal structure with device performance to better understand this effect. Figure 4A-4D displays the

distribution of contact potential difference (CPD) under dark and illuminated conditions for the control and target samples. The experimental setup is illustrated in Figure S31. The surface photovoltage difference (ΔSPV = CPD_{dark} - CPD_{light}) for the target sample (101 mV) is lower than that of the control sample (331 mV), indicating a relatively small change. This suggests that the accumulation of photo-excited holes at the surfaces of the target sample is suppressed, resulting in a lesser shift in the holes' quasi-Fermi level towards the valence band, attributed to increased nonradiative recombination.[15] Certainly the control sample also has its own issues, with a large average CPD compared to the target sample. This indicates a higher voltage requirement to balance the work functions of Au and SnO_2 through the perovskite layer, leading to voltage loss (V_{loss}).[16] This is why the random orientation represented by the control device often requires further optimization.

We used surface Kelvin probe force microscopy (KPFM) to deepen our understanding of nonradiative recombination

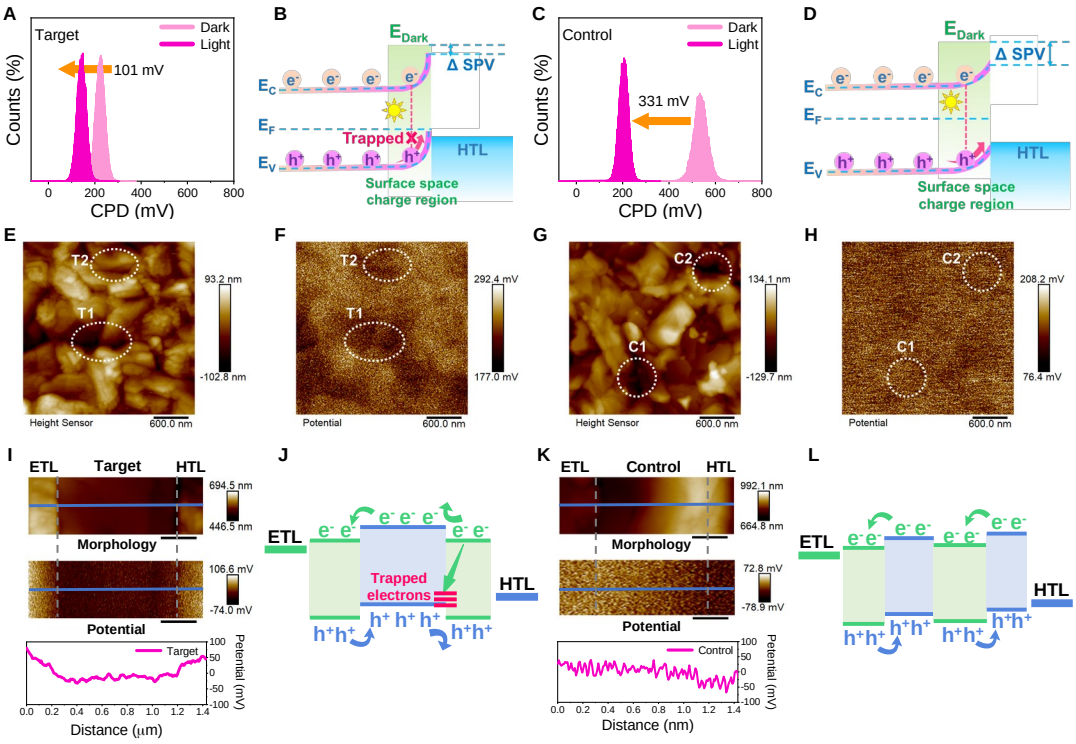

Figure 4. (A-D) Contact potential difference (CPD) distributions in the dark and under illumination for different films, and schematic diagram of surface photovoltage difference (ΔSPV) at the perovskite surface. (E-H) Height and KPFM mappings of perovskite films. The white dashed cycles denote the energetic disorder in the target sample (T1, T2) and control (C1, C2). (I-L) Cross-sectional morphology, potential mapping, and the CPD distribution of different perovskite films with KPFM, and corresponding models for band alignments.

induced by facet heterogeneity (Figure 4E-4H). Compared to the control, the target film exhibits better grain size and surface roughness due to (111)-dominance, along with a narrower CPD distribution (Figure S32). In stark contrast, the relationship between the target surface's energetic landscape and surface morphology is markedly different. By calculating the correlation coefficient R,[17] the potential-morphology correlation of the target sample is increased by nearly an order of magnitude compared to the control sample. Two regions marked by dashed circles in the control sample correspond to local height valleys with flat potential regions, while the target sample highlights two disordered grain structures, appearing consistently in both morphology and potential images. These represent bulk defects, such as distorted GBs or dislocations, which act as non-radiative recombination centers.

Cross-sectional KPFM is further conducted in perovskite film to investigate the cross-sectional potential distribution. As shown in Figure 4I and 4K, the control film displays a relatively stable, straight potential curve, while the target film exhibits a dip in the bulk of the perovskite, with higher potential observed at the surface and bottom regions. By considering the characteristics of each facet, we can better understand this phenomenon. The exposed halogens on the (111) facets provide p-type doping due to negatively charged Pb^{2+} and MA^{+} vacancies, while the exposed cations on the (001) facets act as n-type doping agents.[18] The gradient-mixed (100) facets at the top and bottom form a type-II band alignment at both ends,[19] inadvertently creating a significant energy potential well. This leads to band bending on the perovskite surface and more charge accumulation, which explains why the target devices experience worse device performance. Surface KPFM measurements across the bulk, surface, and buried interfaces of the target film further confirm the existence of an energy potential well (Figure S33). Based on the orientation model, a corresponding diagram of the band alignments was constructed (Figure 4J, 4L).

Relationship Between Facet Distribution and Stability

To validate the impact of facet distribution on the PSCs, we examined the open-circuit voltage (V_{oc}) as a function of scan cycles for both control and target PSCs (Figure 5A, 5B). Herein, to eliminate the influence of other factors, we selected two devices with similar ultimate PCE, maintained a consistent scan rate, and observed that the overall J_{sc} remained relatively stable across increased scan cycles. The V_{oc} generally increased with more scan cycles, which is attributed to the light soaking effect (LSE). [20] LSE often generates by accumulating charge carriers at interfaces and altering the built-in electric field during light exposure. Compared to control devices, target devices exhibited an obvious LSE, likely due to more trap density and ion migration, which affect device stability. The results confirm the accuracy of the relationship within the crystal structure and band alignments we have established. To gain further insights, we

used impedance spectroscopy (IS), a powerful technique for distinguishing between the electronic and ionic responses in perovskite device stacks due to their distinct high frequency (HF) and low frequency (LF) scales, respectively.[21] In Figure 5C, the impedance spectra of the control and target PSCs were measured across a frequency range from 0.01 Hz to 1 MHz, revealing two semicircles in the Nyquist plot representing HF and LF processes. The HF semicircle, associated with recombination resistance (R_{rec}), increased from 1693 Ω in the control device to 1864 Ω after NMP assistance, indicating improved crystallite order. However, the LF response showed time constants of 207 ms and 91 ms, suggesting intensified ion migration in the target devices, which disrupts photoelectric response and appears visual LSE.[22] The Nyquist plot also showed reduced capacitance at 10^{-1} ~ 10^{-2} Hz (beyond the LF range) with a negative hook in Figure S34. This phenomenon is commonly associated with the response of the LSE hysteresis. In practice, the control devices with randomly oriented crystals exhibit hysteresis in their J-V curves, whereas the target devices, characterized by pronounced facet heterogeneity and uneven facet distribution, demonstrate more significant ion migration, resulting in a higher hysteresis index (Figure S35 and Table S5). Although the target devices are predominantly (111)-facet-oriented, the primary origin of hysteresis stems from the inhomogeneous distribution of non-dominant (100) facets.

In addition, both the control and target samples exhibit facet heterogeneity, with an imperfect alignment between the (111) and (100) facets. But the orderly stacking misalignment in target sample creates significant heterogeneous grain boundaries (GBs), as shown in the Figure 5E and Figures S35-S36. Typically, these GBs lead to the degradation of the α-phase into the δ-phase when exposed to air, introducing instability, as illustrated in Figure 5F. Notably, under the target condition, the structure transitions to an unconventional 6H phase rather than the typical 2H phase. This transformation from 2H to the inactive 6H phase further underscores the instability of the target condition. The yellow-phase 6H structure also traps intermediate phases, introducing more non-radiative recombination sites. Detailed

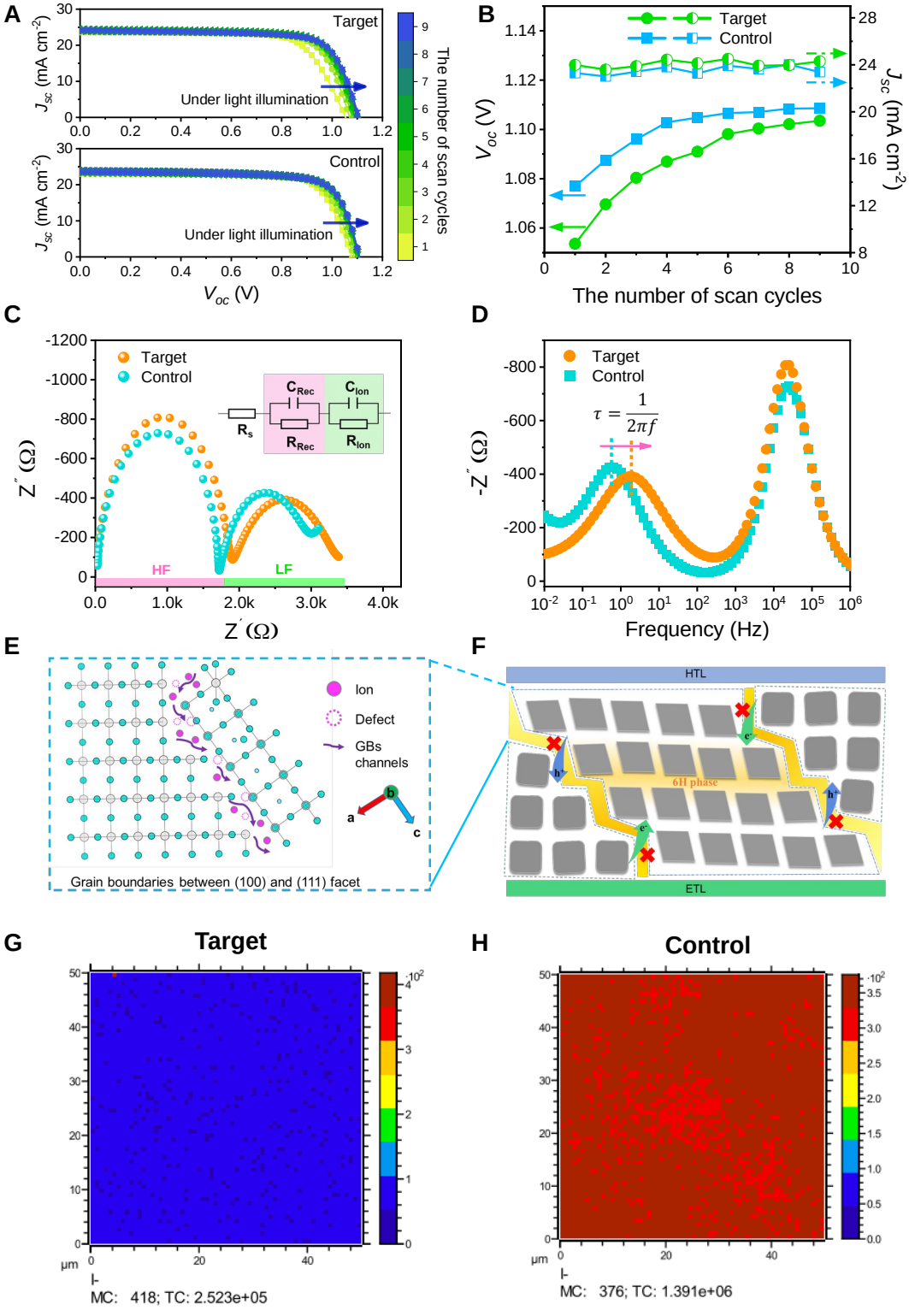

Figure 5. (A) *J-V* plots of different PSCs under 1 Sun illumination, and (B) the corresponding V_{oc} and J_{sc} variation as a function of the scan cycles number. (C) Nyquist plots of the control and target PSCs measured under illumination with a 1000lux white LED at open circuit, and (D) the corresponding plots of the imaginary impedance

against frequency. (E, F) Illustration of GBs channel with charge accumulation and 6H δ-phase in the target film. (G, H) 2D TOF-SIMS mapping of I^- of different unencapsulated perovskite devices aged under 1 Sun illumination for a week.

connection models are shown in Figures S38-S39. The distinction is that the target, enriched with (100) facets on both the top and bottom surfaces, experiences more pronounced obstructions to charge transport under light exposure, with charge accumulation leading to more severe degradation. Conductive atomic force microscopy (c-AFM) on the target film (Figures S40-S41) showed minimal photocurrent variations, with increased leakage current at grain boundaries (GBs),[23] contributing to charge accumulation.[24] Furthermore, EQE and PL measurements corroborate the loss of current, providing additional evidence (Figures S42-S43). Furthermore, compared to the control sample, the target sample exhibits no significant changes in the initial horizontal phase distribution. In stark contrast, the target device undergoes nearly complete degradation after just one week of storage. While the control device, with a random distribution, exhibits better stability. These observations can be elucidated using time-of-flight secondary-ion mass spectrometry (TOF-SIMS) technology to visualize (Figure 5G, 5H and Figures S44-S46).

Solutions to Facet Heterogeneity

Based on our findings regarding the detrimental effects of facet distribution from the perspectives of band alignment and ionic boundaries, it is evident that facet heterogeneity driven by uneven facet distribution is the underlying factor determining device performance. To emphasize this factor, we explored the effect by varying the CsI content to the perovskite composition. In Figure 6A-6B, color-mapped XRD patterns were used to visualize the intensity variations of PbI_2 in the first step and the corresponding (111)/(100) facet ratio of the perovskite in the second step. The magnitude of the variation range induced by compositional tuning effectively reflects the tolerance of solvent regulation to facet heterogeneity—the larger the range, the lower the tolerance, and the less favorable it is for achieving uniform facet distribution. It is observed that ternary solvent regulation strategies easily promote higher (111) dominances in the color mapping, but this comes at the cost of lower tolerance to facet heterogeneity (Figure 6C). Notably, as the mixed solvent ratio increases, the variation in facet ratio becomes more pronounced. In contrast, binary solvent systems (DMF/DMSO or DMF/NMP) exhibit the smaller range of variation, highlighting that even with random orientation under control conditions, a relatively uniform facet distribution aids in tolerating facet heterogeneity. This also demonstrates that the disordering effects induced by solvents should not be simply understood as a disruption of randomized nucleation but rather as a critical factor that exacerbates facet heterogeneity. Additional evidence of solvent-regulation-induced facet heterogeneity can be found in Figures S47-S48.

Furthermore, the peak intensity of PbI_2 does not align completely with the (111)/(100) variation, suggesting another influence from compositional regulation. In addition to adjusting lead iodide and corresponding ammonium salts, composition regulation also involves the introduction of additional additives. Here, cesium trifluoroacetate (CsTFA) was used as a composition additive. We introduced varying molar percentages of CsTFA additives into the target devices to establish a correlation. As shown in Figure 6D and 6E, the addition of CsTFA gradually shifted the orientation from (111)-dominant to (100)-dominant, leading to corresponding changes in PCE. Detailed of photovoltaic parameters are provided in Figure S50. The change in PCE is not a simple improvement but rather first decreases and then increases, showing a distinct trend. We utilized GIWAXS characterization to identify the underlying evolutionary pattern (Figure S51). It can be seen that the intensity variations of the (111) and (100) facets are roughly opposite. When the intensities of both facets are comparable, the PCE reaches its minimum value, coinciding with the peak value of facet heterogeneity in Figure 6F. And the PCE plot clearly shows two distinct equivalent circuits. Subsequently, increasing the CsTFA content made compositional regulation dominate over solvent regulation, ultimately suppressing heterogeneity and achieving a higher PCE than that of the target. This finding is consistent with the rationale behind using additives in traditional literature—introducing appropriate additives can reduce facet heterogeneity. The long-term stability test of the devices also demonstrates improvement (Figure S52). While the target condition enhances the (111) orientation, it simultaneously introduces severe facet heterogeneity. The incorporation of CsTFA effectively mitigates this heterogeneity, and experimental results confirm that facet heterogeneity plays a more critical role in device performance than facet orientation alone. This shift in focus directs our work toward examining the impact of non-dominant facet distribution. Other factors, such as temperature regulation (Figure S53), exhibit similar trends. This study also indirectly challenges the feasibility of utilizing mixed facet heterojunctions in bulk for fabricating solar cells. The concept of utilizing heterofacet structures to drive photocarrier separation remains to be explored (Figure S54).

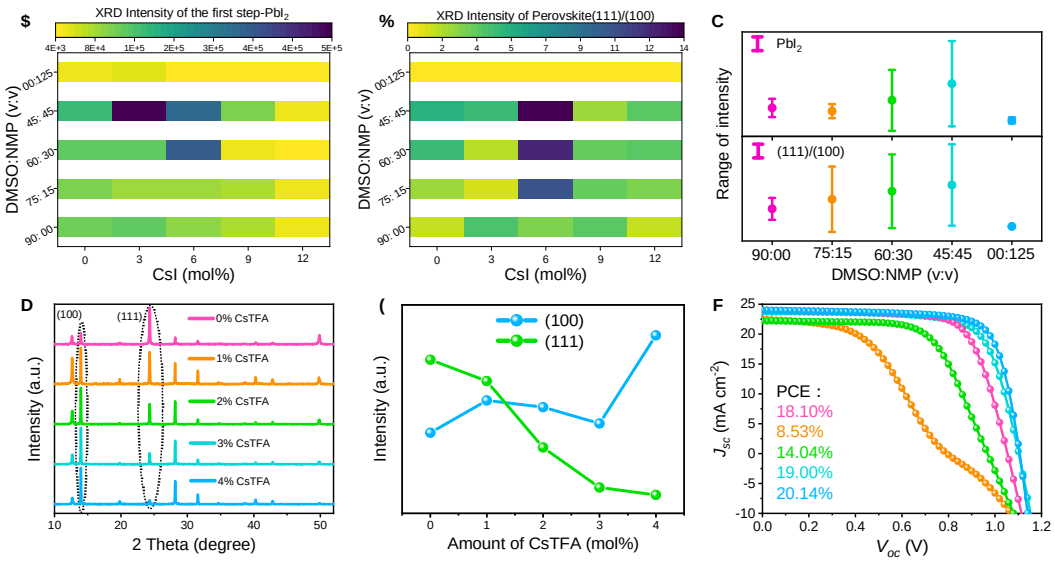

Figure 6. (A-B) The color-mapped XRD pattern of PbI_2 intensity and perovskite orientation as a function of different solvent ratio and CsI amount. (C) The variation range of intensity obtained from Figure 6A-6B. (D, F) XRD patterns in target condition with different additive amount and their corresponding PCEs. (E) The peak intensity about the (111) facets and (001) facets obtained from corresponding 2D GIWAXS patterns.

3. CONCLUSION

In summary, we systematically investigated the overlooked role of non-dominant (100) facet distribution in (111)-dominated perovskite films, demonstrating that facet heterogeneity significantly impacts both PCE and stability. Contrary to the assumption that stacking (111) facets inherently enhances device performance, our findings reveal that charge accumulation induced by the uneven distribution of (100) facets can adversely affect photoelectric property. We established a clear and interconnected relationship between facet distribution and device performance, providing a pathway to enhance the quality of PSCs by strategic facet management. By elucidating the growth mechanism with intermediate phase, this study investigates solvent–orientations interactions, challenging the conventional view that random nucleation is triggered by solvent removal. It reveals that the disordering effects induced by solvents will disrupt facet distribution due to the subsequent uncontrollable crystal growth. Subsequent additive regulation effectively reduced heterogeneity, leading to comprehensive improvements in both PCE and stability. This demonstrates that compared to achieving highly enhanced preferential orientation, regulating facet heterogeneity plays a more crucial role in optimizing device performance. Finally, the study deepens the understanding of the complex interplay between factors influencing orientation, such as composition, temperature, and solvent, providing valuable insights for regulating the facet heterogeneity for uniform perovskite films.

4. EXPERIMENTAL SECTION

4.1. Materials. Anhydrous Dimethylsulfoxide (DMSO, 99.9%), N-methyl-2-pyrrolidone (NMP, 99.9%), and N,N-dimethylformamide (DMF, 99.8%), isopropanol (anhydrous, 99.5%) were purchased from Sigma-Aldrich. Tin oxide nanoparticle colloid precursor (SnO_2, 15% in H2O colloidal dispersion) was purchased from Alfa Asear. Formamidinium iodide (FAI), cesium iodide (CsI), methylammonium iodide (MAI), lead iodide (PbI_2), methylammonium chloride (MACl), phenethylammonium iodide (PEAI), cesium trifluoroacetate (CsTFA, BioUltra, ≥99.0%), 2,2',7,7'-Tetrakis (N,N-di-pmethoxyphenylamine)-9,9'spirobifluorene (Spiro-OMeTAD) were purchased from Xi'an Polymer Light Co. Ltd. 4-tert-butyl pyridine (TBP) and lithium bis(trifluoromethane) sulfonimide (Li-TFSI) were purchased from Shanghai Aladdin Biological Technology Co. Ltd. All these commercially available materials were used without any further purification.

4.2 Preparation for solutions. For the preparation of the PbI_2 precursor solution, PbI_2 (691.5 mg), CsI(13mg) were dissolved in 910 µL of DMF mixed with 90 µL of DMSO to obtain the PbI2 precursor solution for the control (DMF/DMSO). For the DMF/DMSO/NMP ternary solvent, the PbI_2 precursor solution was prepared by partially substituting DMSO with NMP, with the ratios of DMF:DMSO:NMP varying from 910:90:0 to 910:45:45. When the amount of NMP in the ternary solvent system exceeds 45 µL, PbI_2 may precipitate or fail to dissolve completely. Proper adjustment of the solvent ratios is crucial, with the DMF:DMSO:NMP ratios varying from 875:00:125 to 875:60:65. For the DMF/NMP binary solvent, it should be noted that the solubility of NMP for PbI_2 is lower than that of DMSO, so that PbI_2 (599.3 mg), CsI(13mg) were dissolved in 875 µL of DMF mixed with 125 µL of NMP and stirring at 60°C until complete dissolution. For the preparation of the organic ammonium salt precursor solution, a mixture of FAI (90 mg), MAI (6.5 mg), MACl (9 mg), were dissolved in 1 mL IPA with stir at room temperature for 2 h. To prepare the Spiro-OMeTAD solution, 72.3 mg of Spiro-OMeTAD was dissolved in 1 mL of CB, which contained 29 µL of TBP and 17.5 µL of LiTFSI (520 mg/mL).

4.3 Device fabrication. The ITO-coated glass substrate was ultrasound in deionized water, ethanol, isopropanol, and ethanol for 30 minutes each, respectively. The substrate was then dried with a nitrogen gun and treated with ultraviolet ozone for 30 minutes. The SnO_2 precursor solution (1:4 volume ratio of SnO_2 colloidal solution to deionized water) was spin-coated on the ITO glass at 4000 rpm for 30 s, and the corresponding SnO_2 film was annealed at 150°C for 30 minutes. Prior to spin-coating, the substrate was treated with ultraviolet ozone for 20 minutes to improve wettability and then transferred to a glove box. During the first step, the PbI_2 was spin-coated on SnO_2 substrate at 1500 rpm for 30 s and then annealed at 70°C for 1 min. During the second step, the organic salt solution was spin-coated on the room temperature PbI_2

films at 2000 rpm for 30 s. After spin coating, annealing at 90 °C for 30s, 150 °C for 15 min in N_2 atmosphere. Subsequently, for post-fabrication surface treatment, 5mg PEAI were dissolved in IPA and filtered before use, and 80 µL solution was spin-coated on the perovskite films at 5000 rpm for 30 s, followed by annealing at 100°C for 5 min. After cooling to room temperature, 35 µL of the Spiro-OMeTAD solution was spin-coated at 3500 rpm for 30 seconds to form the HTL. Finally, approximately 100 nm of Au was thermally deposited on the Spiro-OMeTAD layer under a pressure of 7×10^{-4} Pa, and the devices were oxidized for 24 hours. The active area of each device was 0.04 cm^2.

4.4 Material characterizations. The ultraviolet-visible (UV-Vis) spectra of the perovskite films were collected using a UV-2600 spectrophotometer. Ultraviolet photoelectron spectroscopy (UPS) measurements were taken using the Thermo ESCALAB 250XI. Pole Figure and Inverse pole Figures (IPF) were used to obtain texture and crystallographic information of films (PANalytical, Smartlab). X-ray diffraction (XRD), grazing incidence X-ray diffraction (GIXRD) patterns of perovskite films were obtained using the Smartlab with a scan rate of 20°/min. Grazing-Incidence Wide-Angle X-Ray Scattering (GIWAXS) data were collected at the Beamline BL14B1 at the Shanghai Synchrotron Radiation Facility (SSRF) using an incident photon energy of 10 keV (wavelength of 1.2398 Å) based on different incident angles and an exposure time of 30 seconds. Scanning electron microscopy (SEM) images and Energy-dispersive spectroscopy (EDS) of the films were captured using the JSM-7800F SEM instrument with an acceleration voltage of 3 kV. Transmission electron microscopy (TEM) were measured using the JEOL JEM 2100F instrument. Atomic Force Microscopy (AFM), conductive-AFM (C-AFM) and Kelvin Probe Force Microscopy (KPFM) were carried out on a Bruker Dimension ICON.

4.5 Device characterizations. Photovoltaic performance measurements were conducted under 1sun intensity (100 mW/cm^2) using a xenon-lamp-based solar simulator (3A, Enli Tech). The intensity of the solar spectrum was calibrated using a monocrystalline silicon solar cell (Enli Tech.). The device was measured in reverse scan (1.2 V→-0.1 V) and forward scan (-0.1 V→1.2 V), with a voltage step of 0.02 V and delay time of 2 ms, using a Keithley 2400 source meter (Keithley Instrument). Electrical impedance spectroscopy (EIS) plotting of all devices was carried out with a frequency range from 10^6 Hz to 0.01 Hz on the Zahner electrochemical workstation. The Nyquist plots of these devices were obtained under dark with an applied bias voltage of 10 mV.

4.6 Computational methods. We constructed the FAI/PbI_2 -terminated (100)/(111) surfaces for $FAPbI_3$ with a vacuum of 20 Å to separate neighboring surfaces in the z-direction. First-principles calculations based on density functional theory (DFT) were carried out using the Vienna Ab initio Simulation Package (VASP).[25] The generalized gradient approximation (GGA) of Perdew-

Burke-Ernzerhof (PBE) functional was employed as the exchange-correlation functional.[26] The DFT-D3 method was adopted for the van der Waals (vdW) correction,[27] and the dipole correction for the slab calculations was applied. The plane-wave cutoff energy of 450 eV was used. The Brillouin zone was sampled using a single gamma point for the (100) surface, and a 2×1×1 mesh grid centered at gamma for the (111) surface. The energy and force convergence criteria were set to 10^{-5} eV and 0.03 eV·Å^{-1}, respectively. The adsorption energies (ΔE_{ads}) of additives with the perovskite surface were calculated as $E_{mol/pvsk} - E_{pvsk} - E_{mol}$, where $E_{mol/pvsk}$, E_{pvsk}, and E_{mol} are the total energies of the adsorption system, the perovskite system and adsorbate molecules, respectively.

ASSOCIATED CONTENT

The Supporting Information is available free of charge via the Internet at http://pubs.acs.org

The detailed information about the characterization techniques including TEM, SEM, EDS, J–V, KPFM, c-AFM, EQE, UV-vis, XRD, GIXRD, Pole figures, Inverse pole figures, GIWAX, PL mapping, TOF-SIM, and Nyquist plots; the experimental results (Figures S1-S54) including diffraction pattern, J−V curves of PSCs, distribution of PV parameters of PSCs, stability test, DFT results, and Tables S1–S5 (PDF)

AUTHOR INFORMATION

Corresponding Author

***Jiewei Liu** – State Key Laboratory of Photoelectric Conversion and Utilization of Solar Energy, Dalian Institute of Chemical Physics, Chinese Academy of Sciences, Dalian 116023, China.

*Email: jwliu@dicp.ac.cn

***Can Li** - State Key Laboratory of Catalysis, Dalian Institute of Chemical Physics, Chinese Academy of Sciences, Dalian 116023, China; University of Chinese Academy of Sciences, Beijing 100049, China;

Orcid: https://orcid.org/0000-0002-9301-7850;

*Email: canli@dicp.ac.cn

Authors

Bo Zhou – State Key Laboratory of Photoelectric Conversion and Utilization of Solar Energy, Dalian Institute of Chemical Physics, Chinese Academy of Sciences, Dalian 116023, China; University of Chinese Academy of Sciences, Beijing 100049, China.

Pei Zhao – Research Center for Computational Science, Institute for Molecular Science, Okazaki 444-8585, Japan. Email:pei@ims.ac.jp.

Junxue Guo – State Key Laboratory of Photoelectric Conversion and Utilization of Solar Energy, State Key Laboratory of Catalysis, Dalian Institute of Chemical Physics, Chinese Academy of Sciences, Dalian 116023, China; School of Chemistry and Materials Science, University of Science and Technology of China, Hefei 230026, China.

Shuaifeng Hu - Clarendon Laboratory, Department of Physics, University of Oxford, Parks Road, Oxford OX1 3PU, U.K.

Xin Guo – State Key Laboratory of Photoelectric Conversion and Utilization

of Solar Energy, Dalian Institute of Chemical Physics, Chinese Academy of Sciences, Dalian 116023, China; University of Chinese Academy of Sciences, Beijing 100049, China.

Notes

The authors declare no competing financial interest.

ACKNOWLEDGMENT

This work was supported by the Strategic Priority Research Program of the Chinese Academy of Sciences (Grant No. XDB1140101). This work was conducted by the Fundamental Research Center of Artificial Photosynthesis (FReCAP), financially supported through National Natural Science Foundation of China (22088102). Bo Zhou gratefully acknowledges Prof. Jie Su (Xi'an University of Electronic Science and Technology) and Prof. Tongle Bu (Wuhan University of Technology) for their generous sharing of the crystal structure file ($PbI_2 \bullet 0.5DMF \bullet 0.5NMP$.cif). Their collegial support and expertise were invaluable to this work.

REFERENCES

(1) Zhang, L.; Mei, L.; Wang, K.; Lv, Y.; Zhang, S.; Lian, Y.; Liu, X.; Ma, Z.; Xiao, G.; Liu, Q.; Zhai, S.; Zhang, S.; Liu, G.; Yuan, L.; Guo, B.; Chen, Z.; Wei, K.; Liu, A.; Yue, S.; Niu, G.; Pan, X.; Sun, J.; Hua, Y.; Wu, W.-Q.; Di, D.; Zhao, B.; Tian, J.; Wang, Z.; Yang, Y.; Chu, L.; Yuan, M.; Zeng, H.; Yip, H.-L.; Yan, K.; Xu, W.; Zhu, L.; Zhang, W.; Xing, G.; Gao, F.; Ding, L. Advances in the Application of Perovskite Materials. *Nano-Micro Lett.* **2023**, *15* (1), 177. https://doi.org/10.1007/s40820-023-01140-3.

(2) *Uniaxial-Oriented Perovskite Films with Controllable Orientation - Li - Advanced Science - Wiley Online Library*. https://onlinelibrary.wiley.com/doi/10.1002/advs.202401184 (accessed 2024-03-18).

(3) Shao, W.; Wang, H.; Ye, F.; Wang, C.; Wang, C.; Cui, H.; Dong, K.; Ge, Y.; Wang, T.; Ke, W.; Fang, G. Modulation of Nucleation and Crystallization in PbI2 Films Promoting Preferential Perovskite Orientation Growth for Efficient Solar Cells. *Energy Environ. Sci.* **2023**, *16* (1), 252–264. https://doi.org/10.1039/D2EE03342A.

(4) Luo, C.; Zheng, G.; Gao, F.; Wang, X.; Zhao, Y.; Gao, X.; Zhao, Q. Facet Orientation Tailoring via 2D-Seed-Induced Growth Enables Highly Efficient and Stable Perovskite Solar Cells. *Joule* **2022**, *6* (1), 240–257. https://doi.org/10.1016/j.joule.2021.12.006.

(5) Liu, J.; Shi, B.; Xu, Q.; Li, Y.; Li, Y.; Liu, P.; SunLi, Z.; Wang, X.; Sun, C.; Han, W.; Li, D.; Wang, S.; Zhang, D.; Li, G.; Du, X.; Zhao, Y.; Zhang, X. Textured Perovskite/Silicon Tandem Solar Cells Achieving Over 30% Efficiency Promoted by 4-Fluorobenzylamine Hydroiodide. *Nano-Micro Lett.* **2024**, *16* (1), 189. https://doi.org/10.1007/s40820-024-01406-4.

(6) Ouyang, Y.; Ou, Z.; Mwakitawa, I. M.; Xia, T.; Pan, Y.; Wang, C.; Gao, Q.; Zhang, B.; Chen, K.; He, Z.; Shumilova, T.; Guo, B.; Zheng, Y.; Jiang, T.; Ma, Z.; Sun, K. Orientation Manipulation and Defect Passivation for Perovskite Solar Cells by a Natural Compound. *Small n/a* (n/a), 2401834. https://doi.org/10.1002/smll.202401834.

(7) Shao, W.; Wang, H.; Ye, F.; Wang, C.;

Wang, C.; Cui, H.; Dong, K.; Ge, Y.; Wang, T.; Ke, W.; Fang, G. Modulation of Nucleation and Crystallization in PbI2 Films Promoting Preferential Perovskite Orientation Growth for Efficient Solar Cells. *Energy Environ. Sci.* **2023**, *16* (1), 252–264. https://doi.org/10.1039/D2EE03342A.

(8) Ma, C.; Kang, M.-C.; Lee, S.-H.; Zhang, Y.; Kang, D.-H.; Yang, W.; Zhao, P.; Kim, S.-W.; Kwon, S. J.; Yang, C.-W.; Yang, Y.; Park, N.-G. Facet-Dependent Passivation for Efficient Perovskite Solar Cells. *J. Am. Chem. Soc.* **2023**, *145* (44), 24349–24357. https://doi.org/10.1021/jacs.3c09327.

(9) Bu, T.; Li, J.; Li, H.; Tian, C.; Su, J.; Tong, G.; Ono, L. K.; Wang, C.; Lin, Z.; Chai, N.; Zhang, X.-L.; Chang, J.; Lu, J.; Zhong, J.; Huang, W.; Qi, Y.; Cheng, Y.-B.; Huang, F. Lead Halide–Templated Crystallization of Methylamine-Free Perovskite for Efficient Photovoltaic Modules. *Science* **2021**, *372* (6548), 1327–1332. https://doi.org/10.1126/science.abh1035.

(10) Harrington, G. F.; Santiso, J. Back-to-Basics Tutorial: X-Ray Diffraction of Thin Films. *J. Electroceramics* **2021**, *47* (4), 141–163. https://doi.org/10.1007/s10832-021-00263-6.

(11) Shin, S.; Seo, S.; Jeong, S.; Sharbirin, A. S.; Kim, J.; Ahn, H.; Park, N.-G.; Shin, H. Kinetic-Controlled Crystallization of α-FAPbI3 Inducing Preferred Crystallographic Orientation Enhances Photovoltaic Performance. *Adv. Sci.* **2023**, *10* (14), 2300798. https://doi.org/10.1002/advs.202300798.

(12) Zhou, Y.; Herz, L. M.; Jen, A. K.-Y.; Saliba, M. Advances and Challenges in Understanding the Microscopic Structure–Property–Performance Relationship in Perovskite Solar Cells. *Nat. Energy* **2022**, *7* (9), 794–807. https://doi.org/10.1038/s41560-022-01096-5.

(13) Zhou, B.; Zhao, P.; Guo, J.; Qiao, Y.; Hu, S.; Guo, X.; Liu, J.; Li, C. Unlocking the Potential of Antisolvent-Free Perovskite Solar Cells: Modulating Crystallization and Intermediates through a Binary Volatile Additive Strategy. *Nano Energy* **2024**, *124*, 109487. https://doi.org/10.1016/j.nanoen.2024.109487.

(14) Li, Y.; Fan, H.; Xu, F.; Wang, T.; Shan, C.; Li, W.; Gu, X.; Lai, X.; Luo, D.; Sun, Z.; Zhao, M.; Li, X.; Cui, K.; Li, G.; Kyaw, A. K. K. High-Performance Inverted Perovskite Solar Cells Enhanced via Partial Replacement of Dimethyl Sulfoxide with N-Methyl-2-Pyrrolidinone. *Sol. RRL* **2022**, *6* (12), 2200816. https://doi.org/10.1002/solr.202200816.

(15) Zhang, C.; Liu, C.; Gao, Y.; Zhu, S.; Chen, F.; Huang, B.; Xie, Y.; Liu, Y.; Ma, M.; Wang, Z.; Wu, S.; Schropp, R. E. I.; Mai, Y. Br Vacancy Defects Healed Perovskite Indoor Photovoltaic Modules with Certified Power Conversion Efficiency Exceeding 36%. *Adv. Sci.* **2022**, *9* (33), 2204138. https://doi.org/10.1002/advs.202204138.

(16) Lee, M.; Choi, E.; Soufiani, A. M.; Lim, J.; Kim, M.; Chen, D.; Green, M. A.; Seidel, J.; Lim, S.; Kim, J.; Dai, X.; Lee-Chin, R.; Zheng, B.; Hameiri, Z.; Park, J.; Hao, X.; Yun, J. S. Enhanced Hole-Carrier Selectivity in Wide Bandgap Halide Perovskite Photovoltaic Devices for Indoor Internet of Things Applications. *Adv. Funct. Mater.* **2021**, *31* (16), 2008908. https://doi.org/10.1002/adfm.202008908.

(17) Meng, H.; Mao, K.; Cai, F.; Zhang, K.; Yuan, S.; Li, T.; Cao, F.; Su, Z.; Zhu, Z.; Feng, X.; Peng, W.; Xu, J.; Gao, Y.; Chen, W.; Xiao, C.; Wu, X.; McGehee, M. D.; Xu, J. Inhibition of Halide Oxidation and Deprotonation of Organic Cations with Dimethylammonium Formate for Air-Processed p–i–n Perovskite Solar Cells. *Nat. Energy* **2024**, *9* (5), 536–547. https://doi.org/10.1038/s41560-024-01471-4.

(18) Ma, C.; Kang, M.-C.; Lee, S.-H.; Kwon, S. J.; Cha, H.-W.; Yang, C.-W.; Park, N.-G. Photovoltaically Top-Performing Perovskite Crystal Facets. *Joule* **2022**, *6* (11), 2626–2643. https://doi.org/10.1016/j.joule.2022.09.012.

(19) Song, K.; Fan, Y.; Qin, W. Structure and Charge Carrier Separation Promotion Effects of Antiphase Boundaries in Cesium Lead Bromide. *J. Phys. Chem. Lett.* **2024**, *15* (8), 2255–2261. https://doi.org/10.1021/acs.jpclett.4c00099.

(20) Lin, L.; Yang, L.; Du, G.; Li, X.; Li, Y.; Deng, J.; Wei, K.; Zhang, J. Light Soaking Effects in Perovskite Solar Cells: Mechanism, Impacts, and Elimination. *ACS Appl. Energy Mater.* **2023**, *6* (20), 10303–10318. https://doi.org/10.1021/acsaem.2c04120.

(21) Hauff, E. von; Klotz, D. Impedance Spectroscopy for Perovskite Solar Cells: Characterisation, Analysis, and Diagnosis. *J. Mater. Chem. C* **2022**, *10* (2), 742–761. https://doi.org/10.1039/D1TC04727B.

(22) Dey, K.; Ghosh, D.; Pilot, M.; R. Pering, S.; Roose, B.; Deswal, P.; P. Senanayak, S.; J. Cameron, P.; Saiful Islam, M.; D. Stranks, S. Substitution of Lead with Tin Suppresses Ionic Transport in Halide Perovskite Optoelectronics. *Energy Environ. Sci.* **2024**, *17* (2), 760–769. https://doi.org/10.1039/D3EE03772J.

(23) Chen, C.; Song, Z.; Xiao, C.; Awni, R. A.; Yao, C.; Shrestha, N.; Li, C.; Bista, S. S.; Zhang, Y.; Chen, L.; Ellingson, R. J.; Jiang, C.-S.; Al-Jassim, M.; Fang, G.; Yan, Y. Arylammonium-Assisted Reduction of the Open-Circuit Voltage Deficit in Wide-Bandgap Perovskite Solar Cells: The Role of Suppressed Ion Migration. *ACS Energy Lett.* **2020**, *5* (8), 2560–2568. https://doi.org/10.1021/acsenergylett.0c01350.

(24) Xu, W.; Gao, Y.; Ming, W.; He, F.; Li, J.; Zhu, X.-H.; Kang, F.; Li, J.; Wei, G. Suppressing Defects-Induced Nonradiative Recombination for Efficient Perovskite Solar Cells through Green Antisolvent Engineering. *Adv. Mater.* **2020**, *32* (38), 2003965. https://doi.org/10.1002/adma.202003965.

(25) Kresse, G.; Furthmüller, J. Efficient Iterative Schemes for Ab Initio Total-Energy Calculations Using a Plane-Wave Basis Set. *Phys. Rev. B* **1996**, *54* (16), 11169–11186. https://doi.org/10.1103/PhysRevB.54.11169.

(26) Perdew, J. P.; Burke, K.; Ernzerhof, M. Generalized Gradient Approximation Made Simple. *Phys. Rev. Lett.* **1996**, *77* (18), 3865–3868. https://doi.org/10.1103/PhysRevLett.77.3865.

(27) Lee, K.; Murray, É. D.; Kong, L.; Lundqvist, B. I.; Langreth, D. C. Higher-Accuracy van Der Waals Density Functional. *Phys. Rev. B* **2010**, *82* (8), 081101. https://doi.org/10.1103/PhysRevB.82.081101.

The Table of Contents